Journal of Materials Chemistry A

Superfast High-Energy Storage Hybrid Device Composed of MXene and Chevrel-Phase Electrodes Operated in Saturated LiCl Electrolyte Solution

Journal:	*Journal of Materials Chemistry A*
Manuscript ID	TA-ART-07-2019-008066.R1
Article Type:	Paper
Date Submitted by the Author:	05-Aug-2019
Complete List of Authors:	Malchik, Fyodor; Bar-Ilan University, Chemistry Shpigel, Netanel; Bar-Ilan University, Chemistry Levi, Mikhael; Bar-Ilan University, Chemistry Mathis, Tyler; Drexel University, Nanomaterials Institute, and Materials Science and Engineering Department Mor, Albert; Bar-Ilan University, Chemistry Gogotsi, Yury; Drexel University, Nanomaterials Institute, and Materials Science and Engineering Department Aurbach, Doron; Bar-Ilan University, Chemistry

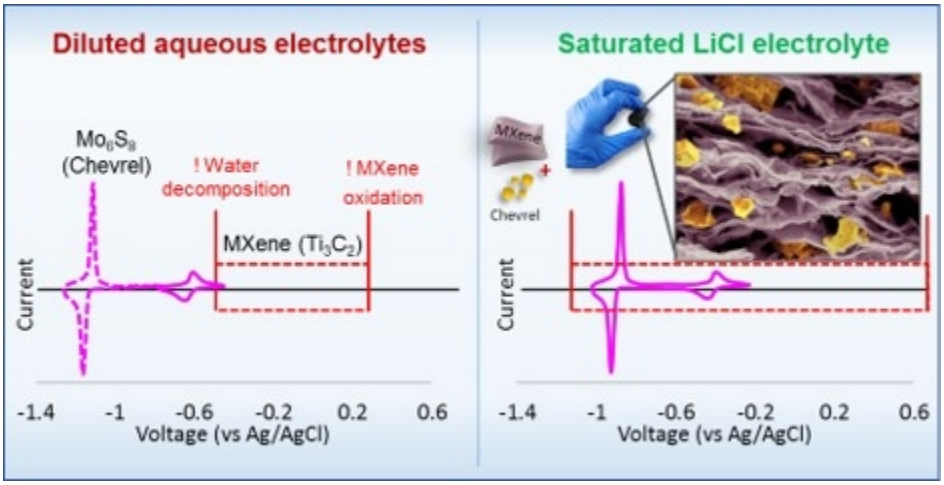

79x40mm (149 x 149 DPI)

Received 00th January 20xx,
Accepted 00th January 20xx

DOI: 10.1039/x0xx00000x
www.rsc.org/

Superfast High-Energy Storage Hybrid Device Composed of MXene and Chevrel-Phase Electrodes Operated in Saturated LiCl Electrolyte Solution

Fyodor Malchik [a], Netanel Shpigel[a], Mikhael D Levi[a], Tyler S. Mathis[b], Albert Mor [a], Yury Gogotsi[b,] and Doron Aurbach*[a]

Development of high power devices with improved energy density is a highly desired target for advanced energy storage applications. Herein we propose a new strategy of triply-hybridized supercapacitive energy storage device composed of hybrid battery-supercapacitor negative electrode [Mo_6S_8 (Chevrel-phase)/Ti_3C_2 (MXene)] coupled with positive nanoporous carbon electrode, integrated with novel yet unexplored saturated (14 M) aqueous solution of LiCl. The electrochemical stability window of this electrolyte solution (2.70 V) significantly exceeds the cell voltage (2.05 V) relevant for the asymmetrical (hybrid anode vs. carbon cathode) cells. The aqeous 14M LiCl solution has far superior characteristics to that of the previously studies 21 m LiTFSI aqueous solution. The paper is also focused on a deep electroanalytical analysis of a peculiar redox/capacitive heterogeinety of hybrid electrodes. It establishes a variety of additivity rules for both differential and integral equilibrium and kinetic characteristics of the charging processes in hybrid electrodes, solving the puzzle of potential distribution of specific electrochemical energy stored the hybrid electrodes. A careful 3-level hybridization design of asymmetric supercapacitive storage devices enabled the integration of battery and supercapacitor materials to get free-standing binderless electrodes suitable for high power/high energy density systems. Studying thoroughly the properties of highly concentrated solutions such as aqueous 14M LiCl, which are very suitable for different types of supercapacitive devices, combined with profound analyses of the properties of hybrid electrodes, will pave the way for a rational design of very effective devices for energy storage and conversion.

Introduction

The ever-increasing need for portable and green energy sources requires development of new electrochemically active electrodes providing high power and high energy densities along with long-term stability. The discovery of 2D Ti_3C_2 (MXenes), an emerging class of 2D transition metal carbides or nitrides derived by selective etching of specific atomic layers (mostly elements from groups 13-16 in the periodic table) has opened new possibilities in terms of fast energy harvesting and storage[1–3]. In recent years, Ti_3C_2 has been the most investigated material due to its high electronic conductivity, impressive mechanical properties[4], and excellent rate capability[1]. The charge storage mechanisms of MXenes strongly depends on the operation environment: in aqueous neutral electrolytes, Ti_3C_2 exhibits purely capacitive-type behavior (capacitances typically about 100 F/g)[5] comparable to that of conventional activated carbon-based supercapacitors. On the contrary, in acidic solutions MXene displays a pseudocapacitive (redox) type behaviour due to surface redox processes occurring between the surface functional groups (such as =O, -OH, and/or -F) and the protons in the electrolyte[6]. Under such conditions, much higher capacitance values, upwards of 380 F/g, can be achieved[7]. Despite the impressive capacitance values and excellent rate capabilities of MXenes, the narrow voltage window (typically up to 1.0 V) significantly limits its energy performance. Irreversible Ti oxidation occurring in the presence of dissolved oxygen at relativity low positive potentials (typically around 0.3 V vs. Ag/AgCl) and hydrogen evolution starting below -0.6 V (vs Ag/AgCl) prevents the operation of MXene beyond this potential range. The suppression of hydrogen and oxygen evolution reactions can be achieved by using highly concentrated aqueous electrolytes (often termed as water-in-salt (WIS) systems), which have much wider electrochemical windows compared to the diluted solutions[8]. However, these super-concentrated electrolytes typically have low conductivity and high production costs. Nevertheless, to the best of our knowledge, the behavior of MXene in these electrolytes has not yet been extensively explored.

[a] *Department of Chemistry and BINA – BIU Center for Nanotechnology and Advanced Materials, Bar-Ilan University, Ramat-Gan 5290002, Israel.*
[b] *Department of Materials Science and Engineering and A. J. Drexel Nanomaterials Institute, Drexel University, Philadelphia, Pennsylvania 19104, United States Address here.*

† Footnotes relating to the title and/or authors should appear here.
Electronic Supplementary Information (ESI) available: [details of any supplementary information available should be included here]. See DOI: 10.1039/x0xx00000x

In contrast to aqueous-based electrolyte solutions, a much wider electrochemical window between 3 V and 5 V can be achieved using aprotic electrolyte solutions[9,10] or ionic liquids[11,12]. However, the rate capabilities of even intrinsically fast battery and supercapacitor electrodes are limited by the poor ionic conductivities of these electrolytes. Hence improvement of the systems using aqueous-based electrolyte solutions, with their high ionic conductivity, can be achieved by integrating typical supercapacitor electrodes, such as MXenes with fast battery electrodes that have larger capacities[10,13,14]. Such integration is only possible if the electrochemical window of the chosen battery material perfectly matches the voltage window of the MXene electrode[15,16]. Note that until recently, all aqeuous asymmetric supercapacitor devices have dealt with neat MXenes as the negative electrode, and carbon or a metal oxide as the positive electrode[17–19]. The main purpose of developing asymmetric devices of this type is to maximize the delivered cell voltage compatible with the electrochemical window of the aqueous-based electrolyte solutions up to 3V [8]. So far, the 2 V cell voltage with MXene negative electrode and a nanoscale carbide-derived carbon positive electrode has been reported for the conventional 1M aqueous solution of Li_2SO_4 (it is important to note that the ohmic potential drops were not accounted for in this work)[18].

Although the electrochemical window of this solution was enough for the successful operation of MXene/nanoporous carbon asymmetrical cell, it appeared to be too narrow for most battery applications. We previously reported that the Chevrel-phase (Mo_6S_8) is an ultrafast negative electrode which can be integrated with positive electrode material $LiMn_2O_4$ (LMO) in a battery using conventional aqueous solution of 2M Li_2SO_4[20]. However, in view of the limited potential window of this electrolyte solution at its negative side, the Chevrel-phase anode was only partially charged

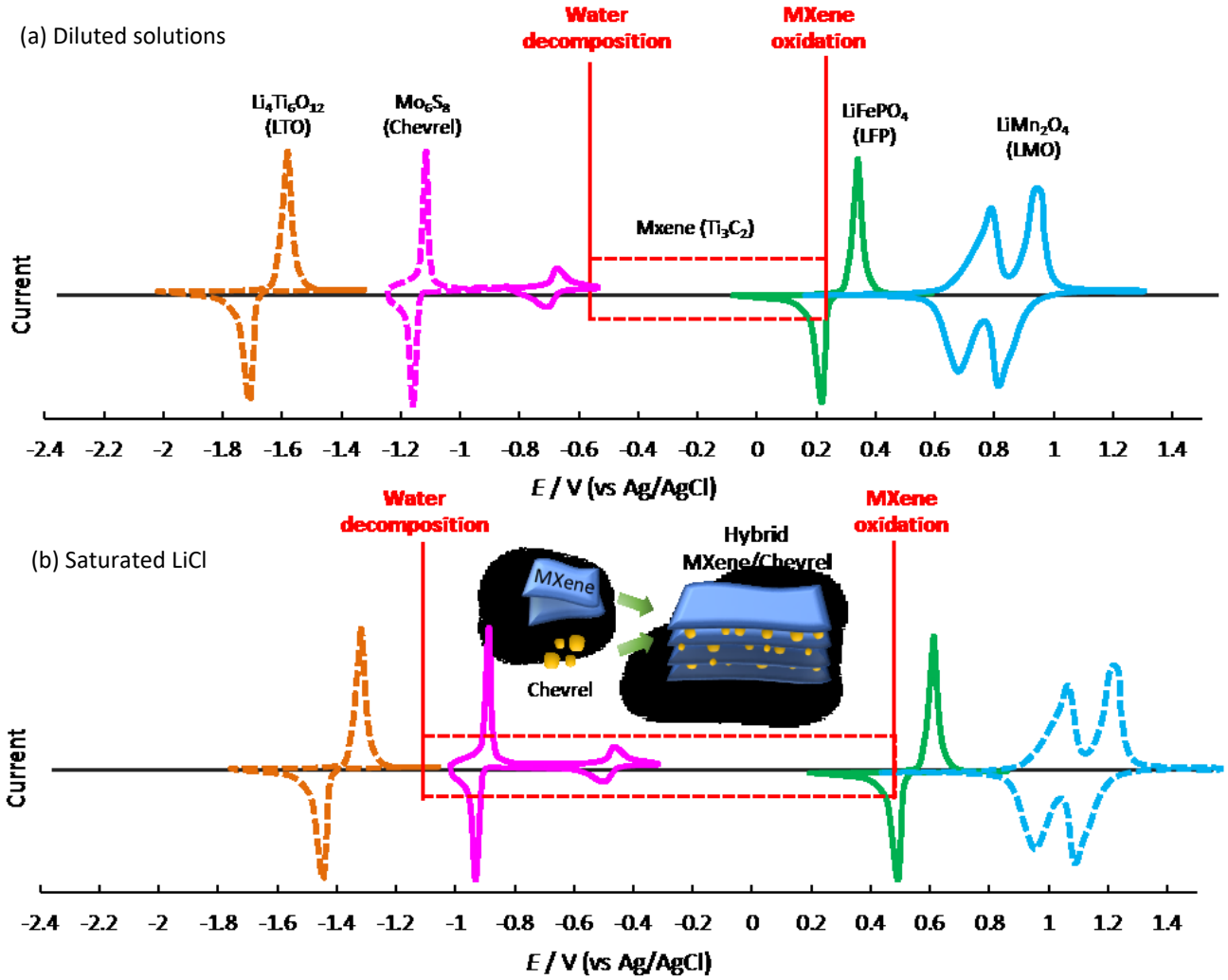

Figure 1: Sketch of the electrochemical windows of typical anodes and cathodes for Li-ion batteries (referenced to Ag/AgCl electrode) for diluted (a) and saturated LiCl solutions (b). The dashed lines correspond to the theoretically expected CV curves if the experimental electrochemical window would not suffer from water decomposition or chlorine evolution. The CVs shown by the solid lines correspond to the selected electrodes located inside the electrochemical window of either diluted or saturated LiCl solutions. The highly concentrated electrolyte solution plays a double role in the hybrid electrodes: (i) it ensures the expanded electrochemical window for the MXene electrodes by suppressing the water activity in the negative potential domain while preventing oxidation of Ti at the potential around 0.6V; (ii) it pushes advantageously the intercalation potential of Li-ions into the Mo_6S_8 towards more positive direction favouring its deep overlapping with intrinsic electrochemical window of the MXene electrodes in saturated LiCl solution.

at a high rate whereas at slow rates of charging the electrode experienced fast self-discharge due to the parasitic reaction of hydrogen evolution.

The problem of limited electrochemical windows of diluted aqueous electrolyte solutions was solved only recently when the same Chevrel-phase/LMO system showed excellent cycling performance in the innovative water-in-salt electrolyte solution containing 5 M (21 moles per kg of solvent) LiTFSI[8]. The wide electrochemical window of this electrolyte of 3 V, having the negative potential limit 1.9 V (vs. Li^+/Li) ensured full charging of the Chevrel-phase electrodes: thus, good cycling performance of 2.3 V Chevrel-phase/LMO aqueous-based battery was successfully demonstrated.

This paper describes two major innovations: One relates to development of integrated (hybrid) Chevrel-phase (Mo_6S_8)/MXene (Ti_3C_2) electrodes, with entirely overlapping intrinsic electrochemical windows, which, in addition, perfectly match the electrochemical stability window of the aqueous saturated (14 M) solution of LiCl. The other innovation is the developed electroanalytical analysis of the characteristic redox/capacitive heterogeneity of hybrid electrodes, proposing the correct solution of the problem of potential distribution of the electrochemical energy stored in hybrid electrodes. The extended electrochemical window of this electrolyte solution (2.7 V) well exceeds the maximal pseudo-equilibrium voltage (2.05 V) of the asymmetrical cell consisting of the hybrid negative Chevrel-phase/MXene electrode and a positive carbon electrode (the ohmic potential drops were subtracted from the cell voltage). The maximal width of the individual voltage window of 1.45 V (vs. Ag/AgCl) was measured for the integrated electrode in a 3-electrode cell. The advantage of using 14.0 M LiCl compared to more diluted solutions becomes clear from two sketches shown in **Fig. 1**. Due to quasi-Nernstian shift of the redox-potential of the Chevrel-phase towards more positive values as compared to that observed in the diluted solutions (panel b versus panel a), the intrinsic electrochemical window of the hybrid electrodes appears to be well inside the extended electrochemical window of the saturated LiCl solution. Note that the integration of Mo_6S_8 particles with the Ti_3C_2 flakes result in optimized hybrid electrodes, in which the MXene sheets simultaneously serve as a conductive binder and as a source of capacitive charge storage. The studied hybrid systems show excellent high energy and power densities (on the scale relevant to capacitive aqueous systems) and can be applied in a practical device which operates in an energy and power range between batteries and supercapacitors. Note that the use of conventional 5 M LiTFSI solutions results in the inferior cycling performance of the hybrid electrodes compared to that in 14 M LiCl because of an order of magnitude lower electric conductivity of the former electrolyte solution.

Results and discussion

Electrochemical windows of LiCl solutions and hybrid Chevrel-phase/MXene electrodes.

It was already mentioned that the relatively low conductivity of 9 mS/cm[8] measured for 5M aqueous-based LiTFSI solution and its high production cost limits its use as a practical electrolyte system

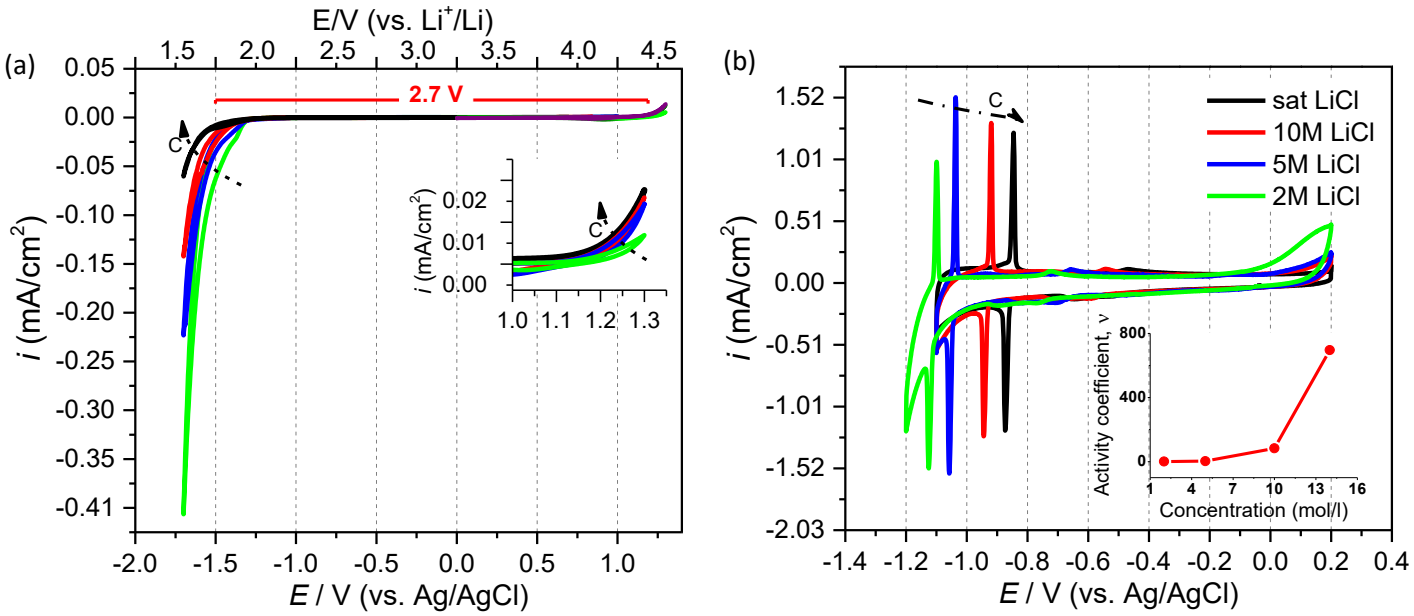

Figure 2: Electrochemical stability window of glassy carbon electrodes in LiCl solutions of different concentrations measured in a 3-electrodes cells (scan rate 10 mV/s), (a). Inset is the enlarged view of the CVs around the positive limit of the electrochemical window. The top horizontal axis shows the potentials recalculated with respect to Li/Li^+ reference electrode. The dashed arrows show the increase of LiCl concentration. (b). CVs measured with hybrid Chevrel-phase/MXene electrodes (containing 10 wt.% Chevrel-phase) in LiCl solutions of different concentrations (scan rate 10 mV/s). Inset presents the activity coefficients for the different concentrations relative to the activity coefficient for the 2M LiCl (for calculation procedure see ref. 8).

for high power application.

On the contrary, saturated LiCl solutions (14.0 M) exhibit much better performance in terms of both conductivity 72.3 mS/cm[21] and lower price. The specific density of this solution is 1.298 g/cm^3 [21] whereas the dynamic viscosity was found to be 16.8 cP[21]. Our measurements of the above three characteristics of 14 M LiCl solution were in good agreement with the literature data.

The electrochemical stability window of the saturated LiCl solutions was first determined using an inert glassy carbon electrode, see **Fig. 2a**. Although the lowest limiting potential of the window, 1.75 V (vs. Li^+/Li) is by 0.15 V more negative than that determined in 5 M LiTFSI (1.9 V), its highest potential limit, 4.45 V, appeared to be less positive than that obtained for the 5 M LiTFSI solution (4.90 V) [8] The opposite dependences of the negative and positive potential limits of the electrochemical window on the concentration changes are clearly seen in **Fig. 2a** (follow the direction of dashed arrows). The *increase* of the LiCl concentration *decreases* the activity of the remaining water, and, hence, *diminishes* the effect of the parasitic process of cathodic hydrogen evolution on the negative potential limit of the potential window. The conclusion about a decreased activity of water in 14 LiCl solution is in a good agreement with the results of *ab initio* molecular dynamic characterization of this solution[22]: In view of deficiency of free water molecules in the concentrated solution, the coordination spheres of Li^+ and Cl^- ions overlap *via* water molecules-shared configurations. The high water deficiency does not allow the highly hydrophilic Li-ions to complete their first hydration sheath, and, as a result, the Cl-anions complement the hydration sheath leading to formation of Li^+-Cl^- ion pairs[22]. In the context of our work, the most important result of the molecular dynamic study of 14 M LiCl solution is the conclusion about a significant decrease of water activity in this concentrated solution, which, in turn, expands significantly the negative potential limit of the electrochemical window for this solution.

In contrast, as follows from **Fig. 2a**, LiCl in a high concentration *shortens* the positive potential limit of the electrochemical window due to enhancement of the parasitic effect of Cl^-- anion electrooxidation (chlorine evolution). Nevertheless, the resulting electrochemical stability window of 2.7 V is wide enough to perfectly match both the intrinsic potential window of hybrid electrode (1.45 V, see **Fig. 2b**), and the entire voltage window of the two-electrode cell comprising negative Chevrel-phase/MXene electrode and positive carbon electrode (2.05 V as will be presented later).

The behavior of the hybrid Chevrel-phase/MXene electrodes in solutions of LiCl of different concentrations is shown in **Fig. 2b**. The contribution of the Chevrel-phase component to the total current is expressed by sharp cathodic/anodic peaks (the left part of the curve) whereas the capacitive rectangular-shape curve is ascribed to the MXene component (the right part of the curve). It is seen that as the concentration of LiCl increases from 2 to 14 M LiCl (see the dashed arrows), two prominent features are seen on the related CVs. This redox-potentials of the Chevrel-phase electrodes (approximated by the cathodic/anodic middle peak potentials), shift towards more positive values, hence decreasing the parasitic contribution of the hydrogen evolution reaction in the vicinity of the negative limit of the electrochemical window. This allows

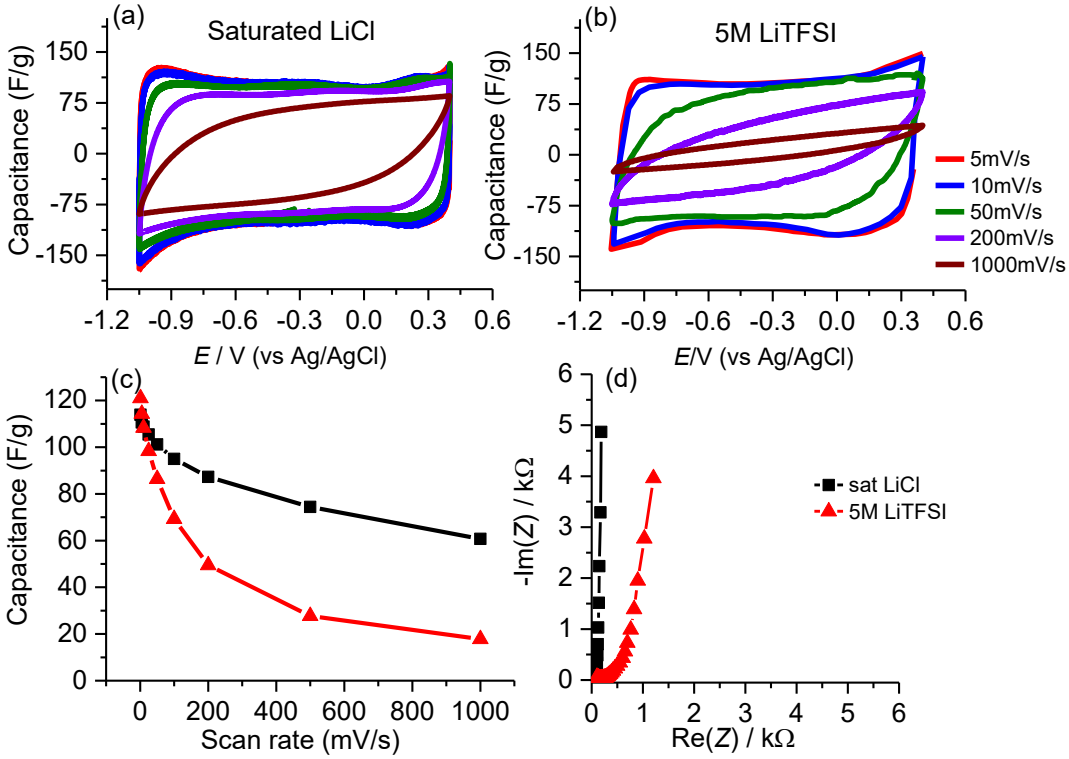

Figure 3: CVs of MXene electrodes recorded at different scan rates in saturated LiCl (a) and in 5M LiTFSI (b). The rate capabilities of MXene for both electrolytes are presented in panel (c). Nyquist plots for the saturated LiCl and 5M LiTFSI solutions (the frequency range extended from 200 kHz to 20 mHz) demonstrate much better conductivity and higher capacitance of the electrodes in the LiCl compared to that in the LiTFSI based electrolyte solutions.

complete charging of the Chevrel-phase components of the hybrid electrodes in the concentrated LiCl solutions. At the same time, the anodic limit of the electrochemical stability window which is controlled by over-oxidation of the MXene component is significantly improved in highly concentrated LiCl solutions due to the suppression of the activity of the remaining water molecules. The relative activity coefficients of the Li-ions were calculated from the deviation of the cathodic/anodic middle-peak potentials (i.e. formal redox potentials of the Chevrel-phase component) in the concentrated solution from that in diluted solutions using the Nernstian-type dependencies of formal redox potentials as a function of the logarithmic concentration as detailed elsewhere[8]. It is seen that the activity coefficients dramatically increase when approaching the saturated LiCl solution correlating thereby with the decreased water activity.

A comparison of the electrochemical performances of pure MXene electrodes operated in saturated LiCl and 5M LiTFSI electrolyte are shown in **Fig. 3.** As can be seen from the CVs (panels a and b), both electrolytes are able to provide a wide intrinsic electrochemical window for the MXene electrodes, about 1.4 V, also showing similar capacitance values for relatively slow charging rates. At higher scan rates (starting from 50 mV/s) the advantage of the LiCl over the LiTFSI solution becomes much more pronounced, as seen in the higher specific capacitance values (**Fig. 3c**). This trend is also evident in the respective impedance spectra, in which the MXene electrodes in 5M LiTFSI exhibit a slopping line in the low frequency domain, in contrast to the almost vertical capacitive line obtained in 14 M LiCl (**Fig. 3d**). As is well-known[15] slow scan rates cyclic voltammertry probes typically quasi-equilibrium state of charged battery and supercapacitor electrodes whereas the electrochemical impedance reflects (in addition to quasi-equilibrium states assessed at very low frequency) a variety of more rapid kinetic steps preceding establishment of quasi-equilibrium. MXene electrodes have typically hierarchical meso/nanoporous structure: the intercalated ions are accommodated in the MXene interspaces whereas the entire MXene electrodes bulk contains many mesopores filled with the electrolyte solution[16]. The role of these mesopores is extremely important in controlling the rate of the electrodes charging since they transport ions from the solution bulk to the MXene interspaces. A poorer conductivity of the 5M LiTFSI compared to that of 14 M LiCl is at the origin of the slower charging of the meso/nanoporous MXene electrodes in LiTFSI compared to LiCl solution in agreement with the impedance spectra for the two electrolytes shown in **Fig. 3d**.

Fig. 4a compares the behavior of the MXene electrode in diluted (1M) and saturated LiCl electrolyte solutions. While for a diluted solution, oxidation of the MXene starts at around 0.3 V revealed by sharp current changes, and hydrogen evolution is seen at -0.5 V. For the saturated LiCl, an almost symmetrical rectangular shape of the CV was observed, which is attributed to a purely capacitive response. In addition to the potential window expansion, the use of super-concentrated LiCl solution allows integration of a battery material with Ti_3C_2. As previously demonstrated in **Fig. 1** using standard Li solutions (mostly of 1M or 2M concentration), none of the commonly used Li battery electrodes falls inside the operational electrochemical window of MXene. As can be seen from **Fig. 4b**, the use of saturated LiCl provides a 280 mV quasi-Nernstian shift of the intercalation potential of the Chevrel-phase electrodes towards the overlap with the electrochemical window of the MXene electrodes. Under these conditions, two clear intercalation/deintercalation peaks are observed originating from the insertion of Li-ions into the different host sites of the Mo_6S_8 structure. The first peak relates to the insertion of one Li-ion ($Mo_6S_8 + Li+ + e- = Li_1Mo_6S_8$) while the second peak corresponds to the insertion of two additional Li-ions to form $Li_3Mo_6S_8$ phase ($Li_1Mo_6S_8 + 2Li+ + 2e- = Li_3Mo_6S_8$)[16]. Previous studies conducted in diluted aqueous Li_2SO_4 demonstrated fast charging capabilities of the Chevrel-phase electrodes, however, only the first reduction peak (related to $Li_1Mo_6S_8$) could be reached due to the limited stability of the electrolyte[13]. The impressive fast and full charging of the Chevrel-phase electrodesin 14 M LiCl is very advantageous for optional integration with the MXene electrodes which also have high rate capability.

Preparation and characterization of hybrid MXene/Chevrel-phase electrodes.

Fabrication of binder-free hybrid Ti_3C_2/Mo_6S_8 electrodes differs significantly from that of conventional composite battery electrodes. The first step of hybrid electrodes preparation is a thorough mixing of aqueous suspensions containing MXene nanoflakes and Chevrel-phase particles in ultrasonic bath. The latter were obtained by sedimentation of as-synthesized Chevrel-phase powder in distilled water selecting a fraction of particles with an average size below 500-600 nm. The mixed suspensions are then vacuum-filtered through a PVdF membrane of known diameter (47 cm). After several hours of drying under vacuum (at 80°C), the filtrated film was peeled off the supporting membrane to get a free-standing hybrid electrodes. To find an optimal Chevrel-phase to MXene mass ratio which is able to deliver the highest power and energy density while maintaining good mechanical properties, several electrodes with different Chevrel-phase mass percentages (10, 30, 50 and 70%) were fabricated while keeping constant mass of MXene. We used the same volume (and mass) of MXene dispersion to which weighed amounts of Chevrel-phase particles were added to change the MXene to Chevrel-phase mass ratio.

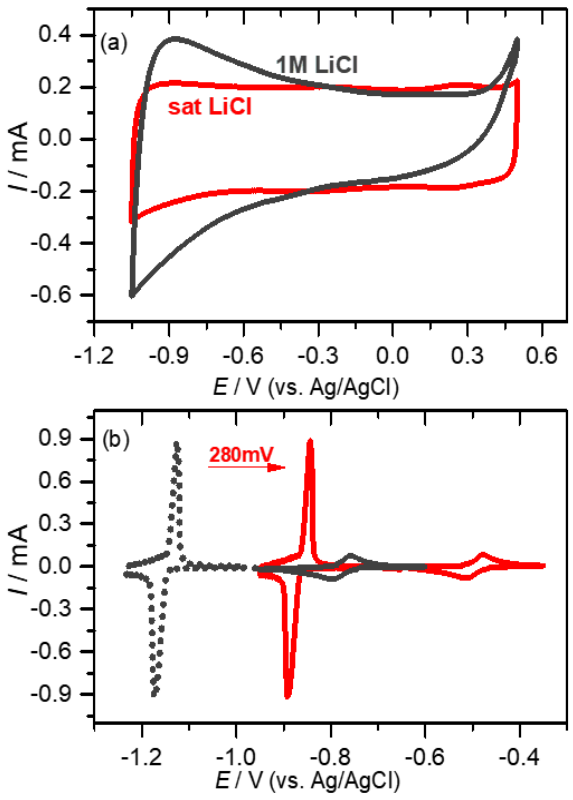

Figure 4: Cyclic voltammograms of neat MXene (a) and Chevrel-phase (b) electrodes operated in diluted and saturated LiCl (grey and red colours, respectively), measured at 5 mV/s. The (theoretically) expected location of the 2nd Li intercalation peak in diluted LiCl is marked by the dotted line.

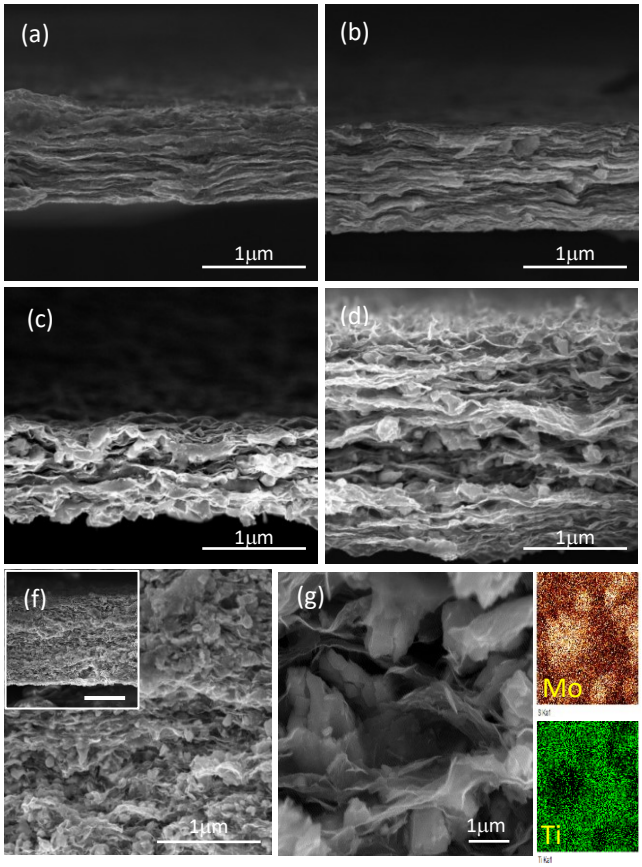

Figure 5: Cross-section images of (a) pure MXene electrodes and for 10%, 30%, 50% and 70% Chevrel-phase component of hybrid electrodes (b to f), respectively. The thickness of the 70% electrodes is shown in the inset of panel f (10µm scale bare). (g) Larger magnification of the hybrid electrodes and the corresponding EDX elemental maps.

Fig. 5 displays cross-section images of pure MXene (panel a) arranged in a multi-layered structure (SEM and XRD pattern of Chevrel-phase are displayed in **Fig. S1**). Panels b-f show the hybrid MXene/Chevrel-phase electrodes obtained for different Chevrel-phase loading (from 10 to 70% shown in panels b-f respectively). The embedded Chevrel-phase particles (average size of 500 nm) can be clearly recognized evenly distributed between the MXene sheets which is also evident from the EDX elemental mapping shown in **Fig. 5g**. The strong interactions between the MXene layers[23] provide an effective binding method for encapsulating the Chevrel-phase particles to form flexible free-standing films. Nevertheless, at 70% Chevrel-phase mass content, the freestanding electrodes lose their flexibility, and poor electrochemical performance was observed due to the high resistivity of the electrodes which significantly deteriorated the electrodes' rate capability (**Fig. S2**). For this reason, we decided to not include it for further data presentation.

The CVs of the hybrid electrodes obtained for different compositions of MXene/Chevrel-phase electrodes are shown in **Fig. 6.** At relatively low scan rates (e.g. 5 mV/s) the combined current – potential response of the hybrid electrodes consists of a typical capacitive rectangular-shaped response of the MXene component, and two sharp redox peaks characteristic of the Chevrel-phase component (panel **a**). As the amount of the added Chevrel-phase particles increases to 50%, the hybrid electrodes thickness also increases, resulting in enhanced electrodes resistivity not only because the electrodes become thicker but also since the MXene matrix becomes deficient in mass as compared to that of Chevrel-phase. Additionally, the distribution of MXene becomes non-continuous with respect to the incorporated Chevrel-phase particles. This results in broadening of the intercalation peaks causing also a larger potential peak separation. Indeed, the conductivity of this 50% hybrid film as measured by 4-point probe, was found to be significantly lower (206 S/cm) than that for 10% and 30% Chevrel-phase loaded electrodes (978 S/cm and 802 S/cm respectively). The cyclic voltammograms measured for 10%, 30%, 50%, and pure Chevrel-phase electrodes are presented in **Fig. 6b, c, d,** and **Fig. S3**, respectively. While at slow scan rate (up to 10 mV/s) two sharp intercalation peaks appear at -0.56 V and -0.86 V, when moderate charging rates were applied (50 mV/s), the peaks become broader due to the limitation by the solid-state diffusion of the Li ions. Under fast charging (500 mV/s), no insertion peaks of the Chevrel-phase electrodes were observed (due to the kinetic limitation of Li insertion into the Mo_6S_8 structure), and the stored charge originates only from the MXene component.

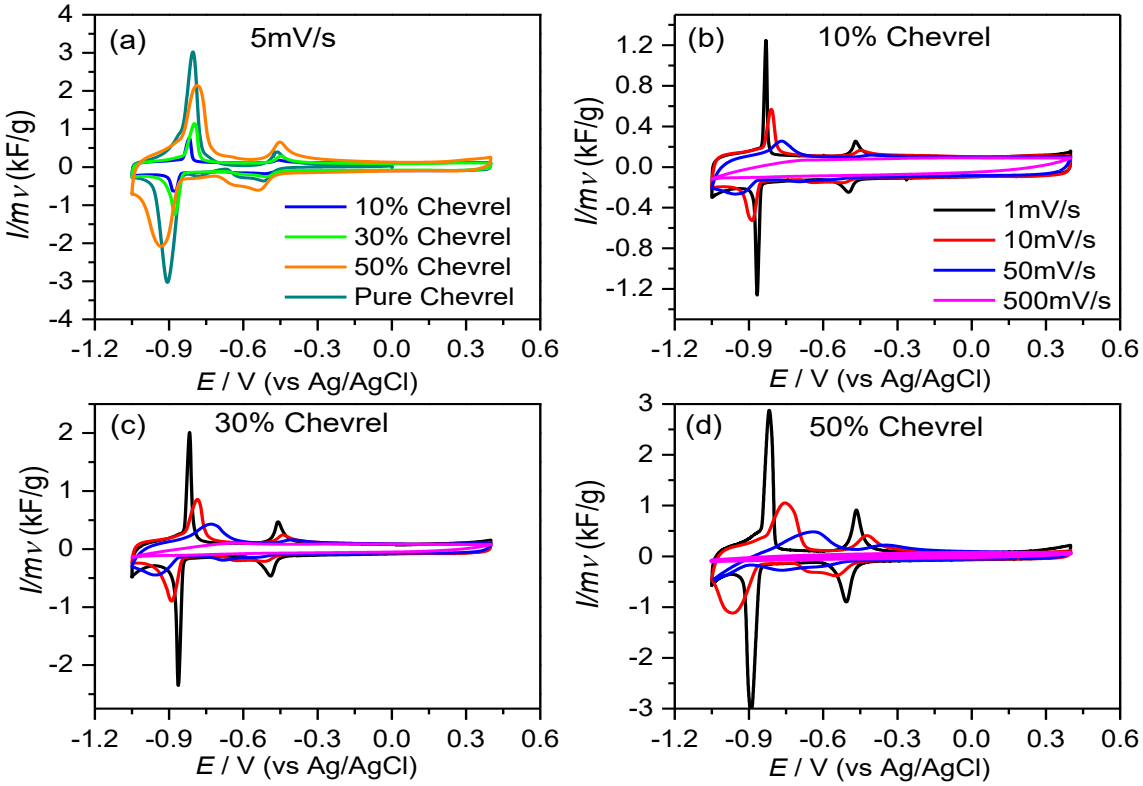

Figure 6: CV curves for neat Chevrel-phase and hybrid MXene/Chevrel-phase electrodes obtained at a scan rate of 5mV/s (a), and at different scan rates (as indicated) for 10%, 30% and 50% systems (b-d respectively). As the scan rate increases the contribution of the battery (Chevrel) component becomes less pronounced and the response turned into the capacitive one.

The effect of the Chevrel-phase-to-MXene mass ratio on the total capacitance is also demonstrated by the galvanostatic curves obtained at relatively small current densities (**Fig. 7a**), showing a mixed battery-supercapacitor chronopotentiometric charging profile. The observed response is characterized by a pure capacitive response in the range of positive potentials expressed by a sloping straight line, followed by two distinguishable plateaus in the vicinity of the lithiation/delithiation potentials attributed to the coexisting two $Li_xMo_6S_8$ phases[24]. With increasing current density from 1 to 50 A/g (**Fig. 7b** and **c**) the time of charge/discharge of the electrodes decrease, and the plateaus associated to the Chevrel-phase component of the hybrid electrodes gradually disappear leaving the

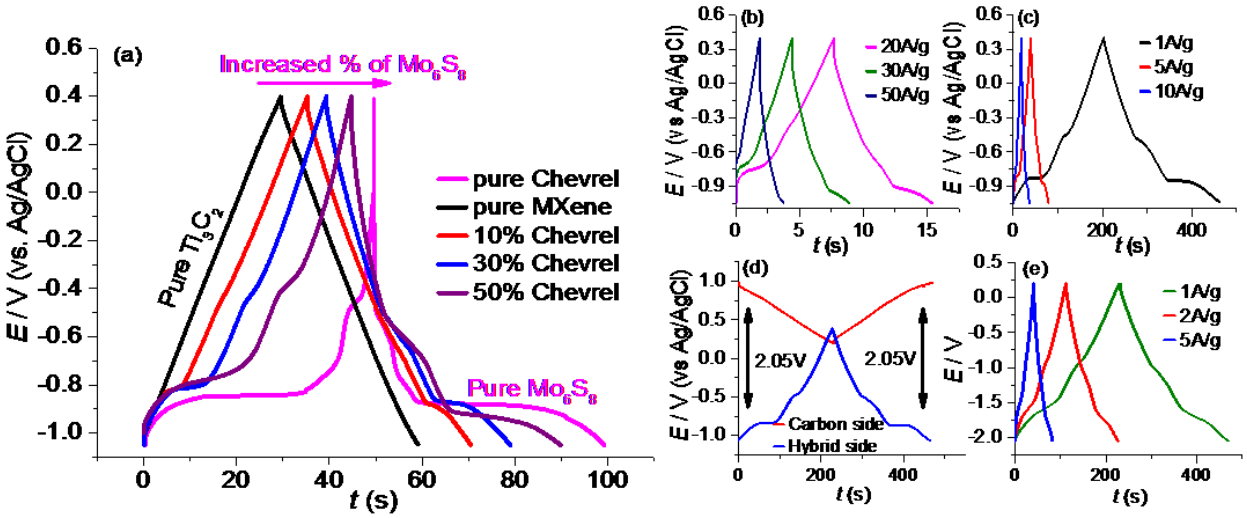

Figure 7: (a) Galvanostatic charge/discharge curves for all the examined systems obtained at a current density 5A/g, and (b and c) for 30% Chevrel-phase content under various current densities. The measurements related to (a-c) were performed in 3-electrode cells; (d) the individual potentials of the MXene/Chevrel-phase anode and the activated carbon cathode measured vs. Ag/AgCl electrode in the operating hybrid/carbon 2-electrode (full) cell, (e) relates to the galvanostatic charge/discharge curves measured in 2-electrode cells at different current densities for 30% Chevrel-phase loaded electrodes.

response to be close to that of the neat MXene component.

Among all the examined compositions, an optimal ratio of 30% Chevrel-phase was found, which showed improved electrochemical performance, in particular, better rate capabilities and relatively high capacitance values demonstrating simultaneously good mechanical properties. **Fig. 7b** and **c** display galvanostatic charge-discharge curves for the 30% Chevrel-phase hybrid electrodes obtained at different current densities in 3-electrode cells. To validate the concept presented herein, the electrochemical performance of this hybrid system was tested using a properly balanced full cell in which activated carbon (YP-50, Kuraray, Japan, see SEM image in **Fig. S4**) was used as the positive electrodes to maximize the output voltage of the cell (**Figs. 7d** and **e**). In order to monitor the individual potentials of the hybrid negative electrodes and the carbon positive electrodes during full 2-electrode cell polarization, the reference electrode was introduced to monitor individual potentials of the negative and positive electrode during the galvanostatic operation in the 2-electrode cell (**Fig. 7d**). Under this configuration, the maximal cell voltage amplitude, 2.25 V at *t*=0 (**Fig. 7e**) is by 0.2 V larger than the difference of the potentials of the individual negative and positive electrodes (i.e. taken vs. reference electrode), 2.05 V (**Fig. 7d**). Note also that the deconvoluted voltage profile of the hybrid electrode (blue line in **Fig. 7d**) is close to that measured in 3-electrode cells at the same current density (black curve in **Fig. 7**c). Three important conclusions can be made from the deconvolution of the cell voltage. (i) To the best of our knowledge the pseudo-equilibrium cell voltage amplitude of 2.05 V is the highest ever reported for a MXene-based

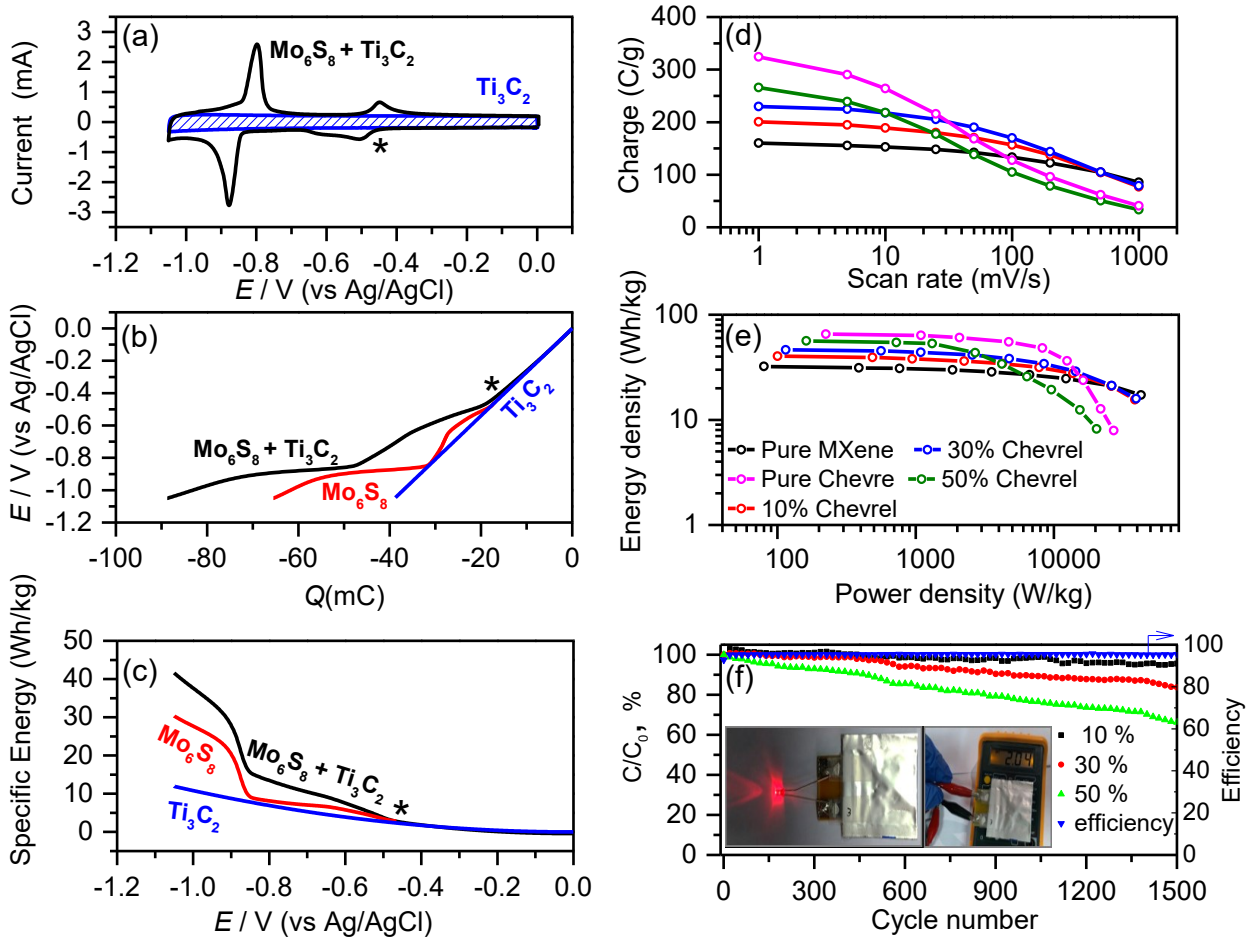

Figure 8: (a) CV of the hybrid electrodes containing 30% of Mo_6S_8 measured in a 3-electrodes cells at a scan rate 5 mV/s (black solid line). CV of the neat Ti_3C_2 electrodes with their mass equal to that containing in the hybrid electrodes is shown by blue curve with hatched area. During reduction from 0 to -0.46 (denoted by asterisk) only Mo_6S_8 component is charged. Further reduction results in simultaneous charging of both the hybrid electrodes components. (b) Integrated CV curve of the same hybrid electrodes presented as *E* vs. *q* plot (black curve). The extrapolated to -1.05 V *E* vs. *q* plot for the Ti_3C_2 component (blue straight line), and the deconvoluted plot for the Mo_6S_8 component (red curve); see text describing the deconvolution procedure. (c) Numerically integrated *E* vs. *q* plots for the hybrid electrodes and their both components representing their specific energies. (d) Variation of the specific capacitance with scan rates for neat and hybrid electrodes (e) Ragone plot for neat and hybrid systems (f) Long term cycling obtained at scan rate of 50 mV/s of hybrid cell containing MXene and 10, 30 and 50% of the Chevrel-phase component as a negative electrode and activated carbon as the positive electrodes. Identical cycling efficiency (>99%, right y-axis) was observed for all the tested electrodes. Inset image: prototype of hybrid MXene/Chevrel-phase device in which activated carbons was used as positive electrodes.

device. (ii) The difference between the pseudo-equilibrium cell voltage and that under polarization in the 2-electrode, i.e. 0.2 V is assigned to the ohmic potential drop in the full cell. (iii) The use of the porous carbon electrodes associated with their high surface area enables reversible adsorption/desorption of chloride anions at the positive potentials demonstrating the full potential window as measured separately for the half cells (**Fig. S5**).

Potential distribution of storable electrochemical energy in hybrid MXene/Chevrel-phase electrodes.

Herein we focus on how the specific energy of the hybrid electrodes is distributed along its entire electrochemical window. For this we assembled cells containing the hybrid electrodes (30% Chevrel-phase) which is charged/discharged using an excessive amount of the carbon counter-electrodes. This implies that the potential of the counter-electrodes does not change during charging/discharging of the working hybrid electrodes (experimentally, the potential of carbon electrodes appeared to be close to that of Ag/AgCl reference electrode). In order to eliminate the limiting effect of ohmic potential drops, these cells were cycled under controlled potential as 3-electrode cells. **Fig. 8a** shows a CV of these electrodes measured at a scan rate v = 5 mV/s. One can easily see that the charge, and hence, the energy density is unevenly distributed across the entire electrochemical window. Down to the potential -0.46 V (denoted by asterisk) the response is perfectly capacitive due to charging of the single Ti_3C_2 component of the hybrid electrodes. However, below -0.46 V down to -1.05 V both Ti_3C_2 and Mo_6S_8 are simultaneously charged: the contribution of Ti_3C_2 is expressed by the rectangular marked in blue color whereas that of Mo_6S_8 manifests by the CV peaks.

During cycling, both components of the hybrid electrodes remain at the same electrodes' potential, E. However, when the potential is swept during the scan, the components of the hybrid electrodes are charged in parallel such that the total charge, q, consists of the sum of the partial charge of the supercapacitor electrodes (Ti_3C_2), q_1, and that of the battery material (Mo_6S_8), q_2:

$$q = q_1 + q_2 \quad (1a)$$

Using linearity property of full differential, we have:

$$\mathrm{d}q = \mathrm{d}q_1 + \mathrm{d}q_2 \quad (1b)$$

Eq. (1a) can be termed additivity rule for the *total* charge of the hybrid electrodes. Differentiating Eq. (1b) with respect to time and potential, we arrive at additivity rule for the total current passed through the electrodes, $I = I_1 + I_2$, and the differential capacitance, $C = C_1 + C_2$, respectively:

$$\frac{\mathrm{d}q}{\mathrm{d}t} = \frac{\mathrm{d}q_1}{\mathrm{d}t} + \frac{\mathrm{d}q_2}{\mathrm{d}t} = I_1 + I_2 \quad (1c)$$

$$\frac{\mathrm{d}q}{\mathrm{d}E} = \frac{\mathrm{d}q_1}{\mathrm{d}E} + \frac{\mathrm{d}q_2}{\mathrm{d}E} = C_1 + C_2 \quad (1d)$$

At any potential, E, within the entire electrochemical window of the hybrid electrodes, the total charge, $q(E)$, can be easily obtained by numerical integration of the CV curves:

$$q(E) = \int \left(\frac{I}{v}\right)\mathrm{d}E = \int C_1 \mathrm{d}E + \int C_2 \mathrm{d}E = q_1(E) + q_2(E) \quad (1e)$$

Whereas Eq. (1a) expresses the additivity rule for the total charge injected into the hybrid electrode, Eq. (1e) allows for deconvolution of the charge of the hybrid electrode at any potential in terms of the partial charges of the supercapacitor and battery electrode components. Since the supercapacitor component is expressed by a rectangular CV (**Fig. 8a**), we can extrapolate the straight-line E as a function of q_1 from 0 till the end of the electrochemical window of the hybrid electrode, -1.5 V (solid blue line in **Fig. 8b**). Starting from the potential -0.47 V (marked by asterisk in **Fig. 8b**, we subtract the value of $q_1(E)$ from the integrated charge, q (E), thus evaluating the charge of the battery component, $q_2(E)$, see solid red line in **Fig. 8b**.

Using the properties of the full differential (Eq. 1b), we can easily arrive at the electrochemical energy related to charging of the hybrid electrodes at any potential, $E_g(E)$, in terms of the sum of the individual contributions from the supercapacitor and battery electrodes, $E_{g1}(E)$ and $E_{g2}(E)$, respectively (additivity rule for the electrochemical energy):

$$E_g(q) = \int E\mathrm{d}q = \int E\mathrm{d}(q_1 + q_2) = \int E\mathrm{d}(q_1) + \int E\mathrm{d}(q_2) = E_{g1}(q_1) + E_{g2}(q_2) \quad (2)$$

When this energy is divided by the mass of the hybrid electrode in kg, and the charges are expressed in Ah, this results in the specific gravimetric energy in Wh/kg.

Note the important division of terms in Eq. (2) allowing for numerical calculation of the energy of the hybrid electrode, E_g and both of its components, E_{g1} and E_{g2} (black, blue and red curves in **Fig. 8c**, respectively). The values of E_g, , E_{g1} and E_{g2} were obtained by numerical integration of E vs. Q curves in **Fig. 8b,** and the charge, q, was transformed into potential, E, based on the curve obtained by integration of the CVs in **Fig. 8a**. It appears that the well-known integral formula for supercapacitor and battery electrodes relating to the entire electrochemical window (E) of the electrode are valid[15]:

For the supercapacitor electrode:

$$E_g = \frac{1}{2} q_1 E = \frac{1}{2} C E^2 , \quad (3)$$

where E denotes the potential of the charged electrode with respect to that of uncharged electrode.

For the battery electrode:

$$E_g = E q_2 , \quad (4)$$

where E denotes the potential of the intercalation-type electrode (usually for intercalation of Li-ions) with respect to the potential of metallic Li-electrode, and q_2 denotes the intercalation charge.

These integral formulas for the specific energy work very well for the neat supercapacitor and battery electrodes, but as seen from Eq. (3) and (4) they have different coefficients (0.5 and 1.0, respectively) preceding the product, $q_{1,2}E$. We checked these formulas for Ti_3C_2 and Mo_6S_8 components applying them to the blue and red curves of E vs. q in **Fig. 8b**. The result is presented in **Fig. S6**: the related values agreed well with that obtained by numerical integration of $E(dq_1)$ and $E(dq_2)$, respectively (see Eq. 2).

However, most importantly, neither of the two conventional Eqs. (3) or (4) valid for the supercapacitor and battery-type electrodes, respectively, can be used to determine the specific energy density of the hybrid electrodes, E_g, because for the entire fixed electrochemical window Eq. (2) is reduced to:

$$E_g = E_{g1} + E_{g2} = \frac{1}{2}CE^2 + Eq_2 \qquad (5)$$

Hence, numerical integration with the use of the left-side of Eq. (2) allows precise calculation of the potential distribution of the specific energy of the hybrid electrodes, and using the additivity rule to perform deconvolution of the total specific energy separating the individual contributions from the supercapacitor and battery components (**Fig. 8c**).

This figure shows very clearly the advantage of using hybrid electrodes in order to increase the energy density of supercapacitors type devices. Indeed, even at the end of the electrochemical window (vertex potential -1.05 V) the energy of the supercapacitor component stored electrostatically remains significantly smaller than the chemical energy of the battery component due to the electrochemically-driven intercalation of Li-ions. The presence of Mo_6S_8 in the hybrid electrodes with Ti_3C_2 significantly increases their energy density. This graph provides a clear rational design of the hybrid electrodes requiring specific conditions for energy delivery as a function of the electrodes potential or time.

Additional practical characteristics of the hybrid electrodes are presented in **Fig. 8d-f**. The rate capability obtained for the different Mo_6S_8/ Ti_3C_2 electrodes compositions is shown in **Fig. 8d** (three-electrode cell configuration). The benefit of the hybrid systems over the neat MXene electrodes consists of providing higher and stable capacities values even at relatively large charging rates. As can be seen for the 10% electrode the specific capacitance of 200 C/g and 85 C/g was obtained at 1mV/s and 1V/s rates, respectively. For the 30% electrodes, the initial specific capacitance of 230 C/g were obtained at 1 mV/s and 85 C/g at 1 V/s. Both 10% and 30% hybrid systems presented almost similar capacitance values at the highest charging rates approaching the capacitance of the MXene components (remember that the electrodes contained the same mass of MXene), since the battery compounds cannot be charged at such high rates.

The superior behavior of the hybrid electrodes is also reflected by the Ragone plots shown in **Fig. 8e**. The large potential window and the high capacitance of the hybrid systems are synergistically combined, exhibiting superior energy and power densities compared to the values observed for the neat compounds (see also **Table S1** comparing capacities, energy and power density of 2 neat components of the hybrid electrodes and the electrodes containing 30% of Chevrel-phase components at scan rates 1 and 1000 mV/s.

It is difficult to compare the performance of the Chevrel-phase/MXene hybrid electrodes in 14 M LiCl with literature data as they refer to quite different systems. Nevertheless, in ref. [8] reporting first on Chevrel-phase/LMO aqueous batteries (5 M LiTFSI solution), the attained capacity of the Chevrel-phase electrodes is between 40-50 mAh/g at 0.15 C rate whereas in our work we reached almost the theoretical capacity of the Chevrel-phase electrodes for a 3 electron process, 90 mAh/g, at 2.5C rate. For MXene negative electrodes cycled with positive electrodes comprising nano-porous carbons in 1M Li_2SO_4 solution (cell voltage 2 V) the specific energy and power were reported to be 27.8 Wh/kg and 1.05×10^4 W/kg, respectively[18]. The hybrid electrodes containing 30 % of the Chevrel-phase components described herein, cycled in 14M LiCl solution within the 1.45 V electrochemical window for the single electrodes reached a higher energy density, 34.2 Wh/kg at a somewhat smaller power density, 0.85×10^4 W/kg. Despite the different nature of these two energy storage devices, the trend of the increase of energy density of the hybrid Chevrel-phase/MXene electrodes compared to that of pure MXene electrodes is evident.

The cycling stability of the hybrid electrodes during long term cycling at 50 mV/s is shown in **Fig. 8f.** After 1500 cycles the capacity retention for the electrodes containing 10% and 30% of the Chevrel-phase components were 95% and 83%, respectively, while a lower retention of 66% was obtained for the hybrid electrodes with 50 % of the Chevrel-phase components (due to the loss of mechanical integrity of the electrode), see **Fig. 8f**. The pure MXene electrode keeps the highest capacity retention of 99% whereas the pure composite Chevrel-phase electrodes containing PVdF binder retain 80% of the initial capacity after 1500 cycles as shown at Fig. S7. It is seen at the low Chevrel-phase content in the hybrid electrodes that the MXene matrix ensures better capacity retention than PVdF does for the composite Chevrel-phase electrodes. Surely optimization of the hybrid electrodes with large content of Chevrel-phase is required to improve mechanical stability of hybrid electrodes. Excellent columbic efficiency (>99%) was observed for all the investigated electrodes. To demonstrate the practical feasibility of the hybrid system, the 30% electrode was assembled into a working device where the activated carbon was used as a counter electrode (see the inset image in Fig. 8f).

Electroanalytical analysis of the redox-heterogeneity of the hybrid electrodes

The integration of Chevrel-phase as a typical battery component with MXene as a capacitive material, provides an ideal model system enabling precise separation between the redox responses and the non-Faradaic (capacitive) contribution to the total charge. This kind of analysis is especially important for pseudocapacitive elements exhibiting rapid (reversible) redox reactions often accompanied by a parallel double layer storage mechanism. Considering the simultaneous presence of two different types of sites on the surface of a supercapacitive electrode due to redox- and capacitive double-layer charging mechanisms, it was proposed that the total maximum CV current measured from this electrode, I_{tot} is equal to the sum of the two related CV currents proportional to the square root of the scan rate (the diffusion-limited domain), and linear with the scan rate (a purely capacitive domain), respectively[25]:

$$I_{tot} = a_{dif}\, v^{b_{dif}} + a_{cap}\, v^{b_{cap}}, \quad (6)$$

where a_{dif} and a_{cap} are the proportionality constants of the diffusion-limited and capacitive domains, respectively, and b_{dif} and b_{cap} are the characteristic power exponents close to 0.5 and 1.0 for the above domains, respectively. There is no doubt that Eq. (6) presents a modified form of Eq. (1c) denoting the additivity rule for the total current. Taking logarithm from both sides of **Eq. (6**) shows that two different limiting slopes, $b_{dif} = 0.5$ and $b_{dif} = 1.0$ will be observed in the range of low and high scan rates, respectively. **Fig. 9** shows the CV current of the hybrid electrode as a function of the increasing scan rate in double log coordinates revealing at least 3 different kinetic domains with the characteristic slopes 0.91, 0.63 and 0.88, respectively (the related CV curves and the values of *a* and *b* values are presented in **Fig. S8** and **Table S2**). In order to assign these slopes to either MXene or Chevrel-phase components of the hybrid electrode, plots of the similar form were built for the pure MXene electrode (the slope is close to 1.0) and Chevrel-phase electrode (0.90 and 0.53 as the scan rate increases). This convincingly shows that the experimental slopes 0.91 and 0.63 of the hybrid electrode relate to the Chevrel-phase component whereas the slope 0.88 characterizes the behaviour of the MXene component in the integrated electrode. The Chevrel-phase as a typical intercalation compound for rechargeable Li-ion batteries has a pseudo-capacitive domain with the characteristic slope 1.0 in the limit of small scan rates which turns into the slope 0.5 at the higher scan rates applied when the slow diffusion of ions in the solid matrix becomes a rate determining step of the entire charging process. From the point of view of formal electrochemical kinetics[26] these two stages are connected in series. Hence the reciprocal of the current related to the charging of the Chevrel-phase component is the sum of the reciprocals of the currents characteristic of the pseudo-capacitive and diffusion domains. This total current related to the Chevrel-phase component is linked in parallel to the current due to charging of the MXene component, formally corresponding to the additivity rule. Hence for the hybrid Chevrel-phase/MXene electrode the total CV current should be represented by a serial/parallel combination of the rates of the related stages:

$$I_{tot} = [\,(a_{pseudo}\, v^{b_{pseudo}})^{-1} + (a_{dif}\, v^{b_{dif}})^{-1}\,]^{-1} + a_{cap}\, v^{b_{cap}} \quad (7)$$

We checked the validity of this formula taking the values of the slopes (*b*) for all the 3 domains indicated in **Fig. 9** together with the

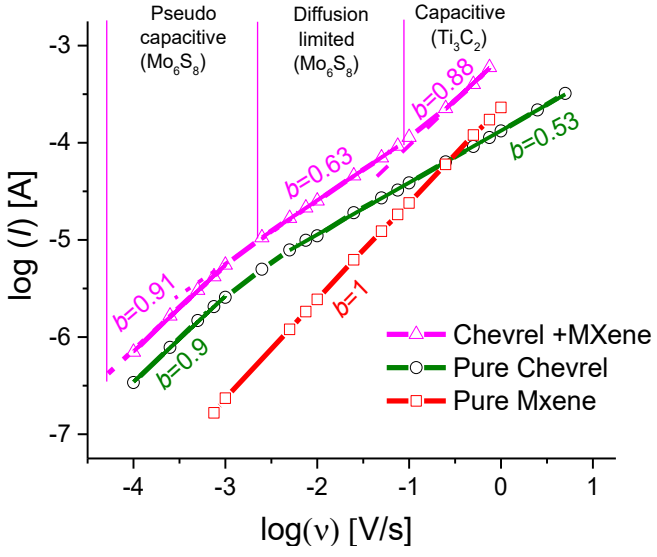

Figure 9: log of the cathodic current peak versus log of the scan rate obtained for neat MXene, Chevrel-phase and hybrid system. The *b* value (i.e. the slope) is indicated.

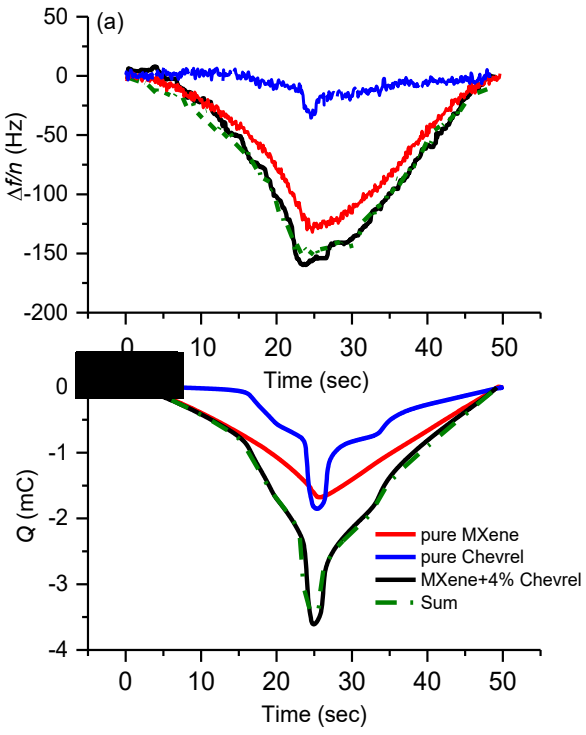

Figure 10 Verification of the additivity rule in integral form for the hybrid electrodes and for its two components with respect to the charge (a) and the frequency change (b) obtained by EQCM-D. The scan rate used was 50 mV/s.

3 intercepts on the Y-axis: the set of the parameters used fits very well the limiting slopes of the pseudo-capacitive and capacitive domains. This is seen From **Fig. S9** which presents simulation of the response of the hybrid electrode obtained with the use of Eq. (7) and the slopes of the individual domains indicated in **Fig. 9**. The diffusion domain of the lower slope is significantly distorted because of the heavy overlap with the neighbouring pseudocapacitive and capacitive domains originating from the Chevrel-phase and MXene components, respectively. Indeed, when further performing numerical calculation we intentionally increased the width of the diffusion domain, three different slopes of all 3 domains became clearly visible (**Fig. S10**). Eq.(7) describing the charging processes in hybrid battery-supercapacitor electrodes is an important extension of Eq. (6) which takes into account the diffusion limitation of charging of the redox-sites but ignores the possibility of their quasi-reversible (pseudo-capacitive) charging in the limit of small scan rates. Hence the hybrid Chevrel-phase/MXene electrodes that allow changes in the mass ratio of the two components provide excellent model electrodes to assess the sites with capacitive, diffusion-limited and pseudo-equilibrium redox types of charging.

Since Eq. (7) relates the total CV current to that due to the components of the hybrid electrodes, the additivity rule for the components in determining the CV current of the hybrid electrodes has been proven in the differential form since the voltammetric current divided by the scan rate represents the differential capacitance (see Eq. (1e)). Earlier discussing **Fig. 8b** we have proved the additivity rule in its integral form, showing that the total charge passed through the hybrid electrodes is the sum of the charges of its both components (Eq. (1a) and (1e)).

Here we report the data showing the correlation between the additivity rule for the charge of the hybrid electrodes and the additivity rule for the resonance width changes of these electrodes measured by EQCM-D. The analysis is greatly facilitated by the fact that the frequency changes, $\Delta f/n$ appeared to be independent of the overtone order, n, and there were no changes in the dissipation factor, i.e. $\Delta D = 0$ (see **Fig. S11**), which proves the gravimetric mode of EQCM-D[[27]]. As shown in **Fig. 10**, the additivity rule is perfectly valid for the charge of the hybrid electrodes and their components obtained by the integration of the related CV curves. The frequency change also follows the additivity rule very well. However, the contribution of the component electrodes into the charge and the frequency change of the hybrid electrodes is different. Whereas both components almost equally contribute to the total charge of the hybrid electrodes (**Fig. 10a**), the frequency change of these electrodes is dominated by the contribution of the MXene component electrodes (**Fig. 10b**). This result is in perfect agreement with our recent report proving that insertion of Li^+-cations into the soft (in thicker layers) MXene electrodes is always accompanied by co-insertion of water molecules which makes the effective mass of the inserted Li^+-cations larger than that for the Li^+-cations entering the perfectly crystalline Chevrel-phase electrodes[28]. Hence, overall, the additivity rule for the hybrid electrodes was strictly proved in its differential, integral and compositional senses.

Conclusions

Saturated aqueous LiCl solution was found to be an excellent electrolyte for charging Chevrel-phase and MXene electrodes, providing one of the widest electrochemical window among the reported aqueous based electrolyte solutions. This allowed for integration of the battery materials, Chevrel-phase, with the capacitive MXene electrodes to fabricate hybrid electrodes for high power and high energy density hybrid devices. The high conductivity of the saturated LiCl enables good electrochemical performance and its relatively low price makes this electrolyte to be a favorable selection over the other water-in-salt solutions such as 5M LiTFSI which has an order of magnitude smaller conductivity than 14 M LiCl solution. The integrated MXene/Chevrel-phase systems were demonstrated to be perfect model systems for quantitative differentiation between the physically different kinetic stages of the charging processes in hybrid electrodes containing both battery and a supercapacitor materials. Using advanced electroanalytical analysis we solved the puzzling problem of the distribution of specific electrochemical energy stored in hybrid electrodes, as a function of the potential applied.

Finally, full flexible cells were constructed using free-standing hybrid electrodes as the anode and the activated carbon as the cathodes to enable a demonstration of 2.05V storage devices. After certain optimization the proposed hybrid electrodes can be applied for high energy and power applications.

Conflicts of interest

There are no conflicts to declare.

Acknowledgements

MXene synthesis and electrochemical characterization at Drexel University was sponsored by the Fluid Interface Reactions, Structures, and Transport (FIRST) Center, an Energy Frontier Research Center (EFRC) funded by the U.S. Department of Energy, Office of Science, and Office of Basic Energy Sciences. Collaboration between Bar-Ilan and Drexel groups was supported by funding from the Binational Science Foundation (BSF) USA–Israel via Research Grant Agreement 2014083/2016. This work has been partially supported by the Israeli Committee of High Education in the framework of the INREP project and by the Israeli Ministry of Science and Technology and Space Grant number 66032. N.S. thanks the Israel Ministry of Science Technology and Space for their financial support.

Notes and references

1 B. Anasori, M. R. Lukatskaya and Y. Gogotsi, *Nat. Rev. Mater.*, 2017, **2**, 16098.

2 X. Zhang, Z. Zhang and Z. Zhou, *J. Energy Chem.*, 2018, **27**, 73–85.

3 J. Pang, R. G. Mendes, A. Bachmatiuk, L. Zhao, H. Q. Ta, T.

Gemming, H. Liu, Z. Liu and M. H. Rummeli, *Chem. Soc. Rev.*, 2019, **48**, 72–133.

4 A. Lipatov, H. Lu, M. Alhabeb, B. Anasori, A. Gruverman, Y. Gogotsi and A. Sinitskii, *Sci. Adv.*, 2018, **4**

5 Y. Dall'Agnese, P. Rozier, P.-L. Taberna, Y. Gogotsi and P. Simon, *J. Power Sources*, 2016, **306**, 510–515.

6 C. Zhan, M. Naguib, M. Lukatskaya, P. R. C. Kent, Y. Gogotsi and D. Jiang, *J. Phys. Chem. Lett.*, 2018, **9**, 1223–1228.

7 M. R. Lukatskaya, S. Kota, Z. Lin, M.-Q. Zhao, N. Shpigel, M. D. Levi, J. Halim, P.-L. Taberna, M. W. Barsoum, P. Simon and Y. Gogotsi, *Nat. Energy*, 2017, **6**, 17105.

8 L. Suo, O. Borodin, T. Gao, M. Olguin, J. Ho, X. Fan, C. Luo, C. Wang and K. Xu, *Science*, 2015, **350**, 938–43.

9 S. Kajiyama, L. Szabova, K. Sodeyama, H. Iinuma, R. Morita, K. Gotoh, Y. Tateyama, M. Okubo and A. Yamada, *ACS Nano*, 2016, **10**, 3334–334.

10 J. Luo, W. Zhang, H. Yuan, C. Jin, L. Zhang, H. Huang, C. Liang, Y. Xia, J. Zhang, Y. Gan and X. Tao, *ACS Nano*, 2017, **11**, 2459–2469.

11 Z. Lin, P. Rozier, B. Duployer, P.-L. Taberna, B. Anasori, Y. Gogotsi and P. Simon, *Electrochem. commun.*, 2016, **72**, 50–53.

12 S. Zheng, C. (John) Zhang, F. Zhou, Y. Dong, X. Shi, V. Nicolosi, Z.-S. Wu and X. Bao, J. Mater. Chem. A, 2019, **7**, 9478–9485

13 Y. Wang, Y. Li, Z. Qiu, X. Wu, P. Zhou, T. Zhou, J. Zhao, Z. Miao, J. Zhou and S. Zhuo, *J. Mater. Chem. A*, 2018, **6**, 11189–11197.

14 X. Guo, X. Xie, S. Choi, Y. Zhao, H. Liu, C. Wang, S. Chang and G. Wang, *J. Mater. Chem. A*, 2017, **5**, 12445–12452.

15 H. S. Choi and C. R. Park, *J. Power Sources*, 2014, **259**, 1–14.

16 W. Zuo, R. Li, C. Zhou, Y. Li, J. Xia and J. Liu, *Adv. Sci.*, 2017, **4**, 1600539.

17 Q. Jiang, N. Kurra, M. Alhabeb, Y. Gogotsi and H. N. Alshareef, *Adv. Energy Mater.*, 2018, **8**, 1703043.

18 J. Li, N. Kurra, M. Seredych, X. Meng, H. Wang and Y. Gogotsi, *Nano Energy*, 2019, **56**, 151–159.

19 A. M. Navarro-Suárez, K. L. Van Aken, T. Mathis, T. Makaryan, J. Yan, J. Carretero-González, T. Rojo and Y. Gogotsi, *Electrochim. Acta*, 2018, **259**, 752–761.

20 M. D. Levi, Y. Shilina, G. Salitra, D. Aurbach, E. Guyot, S. Seghir, J. M. Lecuire and C. Boulanger, *J. Solid State Electrochem.*, 2012, **16**, 3443–3448.

21 K. Tanaka and R. Tamamushi, *Zeitschrift für Naturforsch. A*, 1991, **46**, 141–147.

22 L. Petit, R. Vuilleumier, P. Maldivi and C. Adamo, *J. Chem. Theory Comput.*, 2008, **4**, 1040–1048.

23 J. Come, Y. Xie, M. Naguib, S. Jesse, S. V. Kalinin, Y. Gogotsi, P. R. C. Kent and N. Balke, *Adv. Energy Mater*. 2016, **6**, 1502290

24 M. D. Levi, E. Lancry, H. Gizbar, Z. Lu, E. Levi, Y. Gofer and D. Aurbach, *J. Electrochem. Soc.*, 2004, **151**, A1044-A1051

25 T. Brezesinski, J. Wang, J. Polleux, B. Dunn and S. H. Tolbert, *J. Am. Chem. Soc.*, 2009, **131**, 1802–1809.

26 A. J. Bard and L. R. Faulkner, *Electrochemical methods : fundamentals and applications*, Wiley, 2001.

27 N. Shpigel, M. D. Levi, S. Sigalov, L. Daikhin and D. Aurbach, *Acc. Chem. Res.*, 2018, **51**, 69–79.

28 N. Shpigel, M. D. Levi, S. Sigalov, T. S. Mathis, Y. Gogotsi and D. Aurbach, *J. Am. Chem. Soc.*, 2018, **140**, 8910–8917.